Supplementary Information

Distortion-resistant optical sectioning for precise 3D long-range turbulence measurements

Yuting Xiao [1,2,3,†], Yu Luo[1,2,4,†], Yan Chen[1,2,3,†], Lianwei Chen [1,2,3], Yang Li [1,2,3], Mingfeng Xu [1,2,3], Mingbo Pu [1,2,3,*], and Xiangang Luo [1,3,*]

[1]State Key Laboratory of Optical Field Manipulation Science and Technology, Institute of Optics and Electronics, Chinese Academy of Sciences, Chengdu 610209, China

[2] Research Center on Vector Optical Fields, Institute of Optics and Electronics, Chinese Academy of Sciences, Chengdu 610209, China

[3] College of Materials Science and Opto-Electronic Technology, University of Chinese Academy of Sciences, Beijing 100049, China

[4] College of Future Information Technology, Fudan University, Shanghai 200433, China

*Corresponding authors. E-mails: pmb@ioe.ac.cn; lxg@ioe.ac.cn;

[†]*These authors contributed equally.*

Supplementary Note 1: Real-time 3D measurement architectures

We demonstrate an architecture for real-time long-range turbulence measurements. This framework incorporates beam scanning, focused illumination, turbulent backscattering, and interferometric detection, forming an integrated framework for the three-dimensional spatial profiling of the instrument. As illustrated in Fig. S1a, the system utilizes a vector synthetic wave (VSW) generation module as the light source. The probe location of the VSW within the target volume is tightly synchronized by a computer via two modules: axial focal-plane selection is achieved using a 4f focus-scan module (Fig. S1b), where the internal translation of the focus-scan lens results in a corresponding shift of the focal plane after the telescope. Lateral positioning is governed by an XY angular-scan module to execute a user-defined trajectory (Fig. S1c).

The return signal is separated from the illumination path by the beam splitter and synchronized with the reference signal using an FPGA-based acquisition system. Three-dimensional reconstruction from point-scanning measurements is technically feasible because the full pipeline is well established in laser-scanning microscopy[1], including beam steering, synchronized acquisition, and computational reconstruction. Under such acquisition conditions, the 3D throughput is primarily limited by scan settings, such as pixel dwell time, pixel count, and scan trajectory. The reconstruction of volumetric data from point-scanning signals follows established principles of scanning optical microscopy, ensuring robust spatial registration and signal fidelity. The final 3D volume is resolved as a dot matrix (Fig. S1 d), comprising interleaved samples of subwave 1 and subwave 2 distributed across the scanning depth. We next analyze the temporal resolution limit of single-point measurements. As illustrated in Fig. S2a, two optical components with a frequency offset Δf, interfere to yield an VSW signal with a period T. As illustrated in Fig. S2b, the underlying phase demodulation scheme[2] is illustrated. To evaluate the theoretical limit, we relax hardware constraints by treating dependent overheads as separable additive terms, such as galvanometer inertia, axial focal-tuning latency, and control-loop settling times. Under this assumption, the ultimate sampling throughput is governed solely by the intrinsic SW signal. Figure S2c shows a timing diagram across three consecutive scanning cycles. A standard four-step phase-shifting algorithm limits the minimum time window acquisition time is 9.3 ns, corresponding to $3T/4$.

The phase demodulation me thods discussed in Fig. S2 serve as a theoretical limit. In practical applications, the raw data stream obtained from the APD reaches approximately 4 GB/s. To overcome this throughput challenge, we implemented a hardware-accelerated architecture, achieving real-time phase demodulation and sustained turbulence monitoring. As illustrated in Fig. S3a, the core of this architecture relies on offloading computationally intensive tasks to an on-chip digital signal processing (DSP) engine[3]. Specifically, we designate one signal path as the external reference to synchronize the built-in phase-locked loop (PLL). First, the system locks onto the reference via the PLL to generate quadrature local oscillators, which are mixed with the probe signal to perform precise frequency translation to the baseband. Second, low-pass filters suppress out-of-band high-frequency noise. Finally, a hardware-accelerated coordinate rotation digital computer algorithm performs instantaneous coordinate conversion and outputs the differential phase at a deterministic rate. This approach compresses the data throughput by three orders of magnitude while preserving critical phase information. The extracted data are streamed to a 1 TB internal SSD for long-term storage and simultaneously routed to the host machine for real-time visualization.

Supplementary Note 2: Principle of the VSDI

When the two sub-beams are projected onto the same linear polarization by an a linear polarizer, the resulting spatiotemporal envelope of the interference intensity can be written as:

$$\begin{aligned}\boldsymbol{E}(\boldsymbol{r},t) &= \sum_{j=1}^{2} A_j(\boldsymbol{r}) e^{-i(\omega_j t+\varphi_j)} \\ &= e^{-i[(\omega_1+\omega_2)t+(\varphi_1+\varphi_2)]/2}\left[A_1(\boldsymbol{r}) e^{-i[(\omega_1-\omega_2)t+(\varphi_1-\varphi_2)]/2} + A_2(\boldsymbol{r}) e^{i[(\omega_1-\omega_2)t+(\varphi_1-\varphi_2)]/2}\right]\end{aligned} \tag{S1}$$

where A_i is the projected amplitudes of the i-th sub-beam along the analyser direction. After removing the rapidly oscillating terms and the constant phase factor $e^{-i[(\omega_1+\omega_2)t+(\varphi_1+\varphi_2)]/2}$, the light intensity can be written as Equation (2) in the main text.

We assume that the refractive index of turbulence is close to unity, that is, $n(x+d) \approx n(x) \approx 1$. Therefore, local refractive-index fluctuations introduce an additional phase difference between the sub-beams can be written as:

$$\left[k_1 n(x+d) - k_2 n(x)\right] L \approx kL\left[n(x+d) - n(x) + \Delta k / k\right] \tag{S2}$$

where $k = (k_1 + k_2)/2$ is the mean wavevector magnitude. The term $\Delta k / k$ is small and a constant (i.e., does not vary with turbulence). It can be removed by calibration. Then phase difference can be written as Equation (3) in the main text. Equation (4) in the main text assumes that the phase of the reference synthetic-wave envelope is used as the baseline and is set to zero.

In Equation (5) of the main text, $\left\langle \Delta\varphi(t)^2 \right\rangle$ is defined as the ensemble average of the squared dynamic differential phase:

$$\left\langle \Delta\varphi(t)^2 \right\rangle = \lim_{M\to\infty} \frac{1}{M} \sum_{m=1}^{M} \Delta\varphi_m(t)^2 \tag{S3}$$

where M is the number of independent realizations, and $\Delta\varphi_m(t)$ denotes the differential phase of the m-th realization. Under the ergodicity assumption, we approximate the ensemble average by the temporal variance of $\Delta\varphi(t)$ over a finite time window:

$$\left\langle \Delta\varphi(t)^2 \right\rangle = \sigma_{\Delta\varphi}^2(T_w) = \frac{1}{N-1} \sum_{i=1}^{N} \left[\Delta\varphi(t_i) - \overline{\Delta\varphi} \right]^2 \tag{S4}$$

where T_w is the length of the time window, N is the number of sampling points within the window, i is the sampling index, t_i the time of the i-th sampling point, $\Delta\varphi(t_i)$ is the measured differential phase at time t_i, $\overline{\Delta\varphi}$ is the arithmetic mean of the measured differential phase within the window.

Supplementary Note 3: Spatial resolution analysis

We theoretically analyzed the spatial resolution of VSDI under the Rayleigh criterion using rigorous diffraction theory and a plane-wave expansion formalism[4]. The incident field propagates through the telescope and is focused onto the sample plane. The lateral and axial resolutions of an individual sub-wave are given by:

$$\delta x \approx 1.22 n \lambda f / D \tag{S5}$$

$$\delta z \approx 8 n \lambda f^2 / D^2 \tag{S6}$$

where n denotes the refractive index of the background medium, f is the focal length of the telescope, and D represents the incident beam diameter. Equations (S5) and (S6) show that the lateral resolution scales linearly with focal length, whereas the axial resolution exhibits a quadratic dependence.

Importantly, unambiguous volumetric sectioning requires the separation between the two focal spots to exceed the diffraction-limited resolution of a single sub-wave. As illustrated in Fig. S5, the focal-spot separation d is dynamically controlled by tuning the relative tilt angle θ between the two sub-waves:

$$d = f \sin\theta \quad \text{(S7)}$$

The spatial resolution limits imposed by diffraction and off-axis beam tilting were systematically investigated. To validate the theoretical framework across different sensing distances, the operational parameters were calculated for target propagation lengths of 650 m and 1,050 m, corresponding to target lateral resolutions of 6.6 mm and 10.6 mm, respectively. To validate the theoretical framework, experimental verification was performed over long-range atmospheric propagation links. Guided by the theoretical model, an off-axis tilt angle of approximately 10 μrad was introduced into the synthetic-wave architecture (Fig. S6). As shown in Figs. S7 and S8, the experimentally measured focal-spot intensity distributions in the x-y plane are in close agreement with the theoretical predictions, accurately reproducing both the transverse full width at half maximum (FWHM) and the dual-focal separation d. To quantify the effective axial gating depth, the electric-field cross-sections at discrete longitudinal positions were evaluated using full-wave electromagnetic simulations. The results show that VSDI maintains an effective axial slice thickness of 30 m with a lateral resolution of 6.6 mm over a propagation distance of 650 m (Fig. S9). At a longer distance of 1,050 m, the system achieves a 90 m axial slice thickness with a lateral resolution of 10.6 mm (Fig. S10).

Supplementary Note 4: Comparison between VSDI and FLDI

As shown in Fig. S11**,** C-FLDI relies on intensity modulation ($I \propto \cos(\Delta\varphi)$), where the inherent cosine nonlinearity restricts the unambiguous measurement range to an interval of π/2. The VSDI signal adopts a physically intuitive form, given by $I \propto \cos(\Delta\omega t+\Delta\varphi)$. This phase difference $\Delta\varphi$ can span the full 2π range and is reconstructed by continuously tracking the relative temporal shift Δt. We compared the robustness of VSDI with that of conventional FLDI (C-FLDI). The phase error was quantified by introducing identical background noise into both channels and calculating the root mean squared error (RMSE) of the residual phase. The robustness was evaluated by computing the RMSE over 5,000 independent Monte Carlo trials. The laser power drift was modeled as random amplitude fluctuations uniformly sampled over 40 discrete intervals within the range [0, 0.1] for both channels. Environmental perturbations were incorporated into the simulation using a Gaussian distribution with a standard deviation of 0.01. The RMSE of the C-FLDI architecture increased to approximately 0.1 rad, indicating that direct intensity-based phase retrieval remains highly sensitive to temporal power fluctuations. In contrast, the RMSE of VSDI remained near zero across all drift levels up to 10%, demonstrating the stability of the phase retrieval architecture. This noise suppression originates from the architectural decoupling mechanism, which isolates amplitude fluctuations from the phase channel in the frequency domain.

Supplementary Note 5: Phase power spectral density of turbulence

Real-world atmospheric experiments are inherently difficult to reproduce. To obtain repeatable measurements under controlled conditions. Using a 1.1-km temperature-controlled heated-wire array, we controllably emulate turbulence with different strengths over a broad dynamic range from 10^{-16} $m^{-2/3}$ to 10^{-13} $m^{-2/3}$. The optical platform is deployed 40 m underground to reduce the influence of ground vibration and surface-temperature fluctuations on the measurement system. To evaluate the physical fidelity of the turbulence generator, we analyzed the phase power spectral density (PSD) measured by the VSDI under different temperature conditions. As shown in Fig. S12, the measured phase PSD exhibits a clear power-law decay over the intermediate frequency range of 5-100 Hz. The fitted slopes range from approximately -2.12 to -2.04, indicating Kolmogorov-like scaling behavior of the phase fluctuations generated by the heated-wire turbulence generator. These slopes fall between the canonical -5/3 scaling of 1D scalar spectra and the -8/3 scaling predicted for 1D phase fluctuations under frozen-flow assumptions[5]. The low-frequency region is mainly affected by large-scale convective motion and thermal drift, whereas the high-frequency region is increasingly influenced by instrumental noise and mechanical disturbances. Therefore, the observed intermediate-band power-law behavior provides evidence that the turbulence generator produces atmospheric-like phase fluctuations over the tested temporal scales.

Supplementary Note 6: Cooperative targets

To benchmark the system performance, we employed a high-precision corner cube retroreflector. Figure S13 shows a photograph of the corner-cube retroreflector. The stable return signal provided by the cooperative target enables calibration of the system sensitivity prior to deployment in more challenging non-cooperative diagnostic scenarios.

Supplementary Note 7: Long-term stability measurements

We performed a long-term stability assessment over a 25-minute measurement session. Data were acquired in a discrete steady-state mode, in which measurements were recorded only after the thermal gradient stabilized at each temperature setpoint, using a 10-s integration window (0.1 Hz) to match the acquisition strategy of the TFS. As shown in Fig. S14, the retrieved C_n^2 exhibit strong agreement with the TFS measurements, yielding a coefficient of determination of $R^2 = 0.94$. Figure S15 shows a photograph of the temperature fluctuation sensor.

Supplementary Note 8: Turbulence anisotropic studies

We extend VSDI from a single detection channel to polarization-resolved measurements, enabling long-range sensing of turbulence-induced phase fluctuations in two orthogonal polarization components. At the receiver, the detection signal is recorded on CH2, while the fiber-end signal is simultaneously acquired on CH1 and used as a local reference for heterodyne phase retrieval (Fig. S16 a). Rather than physically separating the polarization components at the receiver, the two polarization channels are digitally demultiplexed. Specifically, the recorded time-domain waveforms are Fourier transformed, and the corresponding heterodyne bands are isolated in the frequency domain to recover the polarization-resolved phases (Fig. S16 b, c).

Using this frequency-domain demultiplexing, we extract the phase fluctuations for the *x*- and *y*-polarized channels, denoted as φ_x and φ_y, together with their differential phase (Fig. S16 d, e). Under different thermal conditions, φ_x and φ_y exhibit highly consistent fluctuation trends, indicating that the measured turbulence response is approximately polarization-isotropic within the sensitivity of our experiment. The differential channel directly quantifies the residual polarization dependence, and its phase variance provides a compact metric for evaluating polarization anisotropy in the turbulence-induced response (Fig. S16 f).

Supplementary Note 9: VSDI vs. other works

Wavefront sensors constitute the mainstream approach for turbulence measurement and have recently been extended to a range of advanced implementations, including metasurface-integrated single-shot wavefront sensors [e.g., *Nature Photonics, 2025, 19:1315-1321.*], wide-field wavefront sensors [e.g., *Nature Photonics, 2024, 18(9): 935-943.*] and large-field-of-view wavefront sensors [e.g., *Light: Science & Applications, 2024, 13(1): 187.*]. Despite extensive progress, the principle for measuring localized turbulence in 3D space remains largely unexplored. Existing methods mainly characterize the cumulative effect of turbulence along the entire propagation path, for example by measuring the final wavefront distortion at the beam terminal. Moreover, most of these approaches lack polarization-measurement capability, making it difficult to comprehensively resolve the 3D dynamic characteristics of localized turbulence. We achieve a kilometre-scale working distance, microsecond temporal resolution, 3D measurement capability and vectorial sensing capability. To further highlight the performance advantages of our method, we systematically summarize the key parameters of this work in Table 1 and compare them in detail with recent related studies for reference.

Table 1. Summary of measurement capabilities vs. other works

Journal	Range	Temporal Resolution	Spatial Resolution	Precision	Dimension
Nature Photonics, 2024, 18(9): 935-943.	750 m	28.71 ms	Lateral: 10 arcsec Longitudinal: 43m	0.21 λ	3D
Nature Photonics, 2025, 19:1315-1321.	< 1 m	10 arcsec	Not specified	Not specified	2D
Light: Science & Applications, 2024, 13(1): 187.	Not specified	Not specified	Lateral: 12.95 μm	0.12 λ	2D
Our work	1,050 m	0.5 μs	Lateral: 1 cm Longitudinal: 90m	1/1000 λ	3D

References

1. Chen, X. *et al.* Artificial confocal microscopy for deep label-free imaging. *Nat. Photon.* **17**, 250–258 (2023).
2. Arnison, M. R., Larkin, K. G., Sheppard, C. J. R., Smith, N. I. & Cogswell, C. J. Linear phase imaging using differential interference contrast microscopy. *J Microsc* **214**, 7–12 (2004).
3. Oppenheim, A. V. *Discrete-Time Signal Processing*. (Pearson Education India, 1999).
4. Born, M. & Wolf, E. *Principles of Optics: Electromagnetic Theory of Propagation, Interference and Diffraction of Light*. (Elsevier, 2013).

5. Onn, F. *Modeling Water Vapor Using GPS with Application to Mitigating InSAR Atmospheric Distortions*. vol. 67 (2006).

Figures and Figure Captions

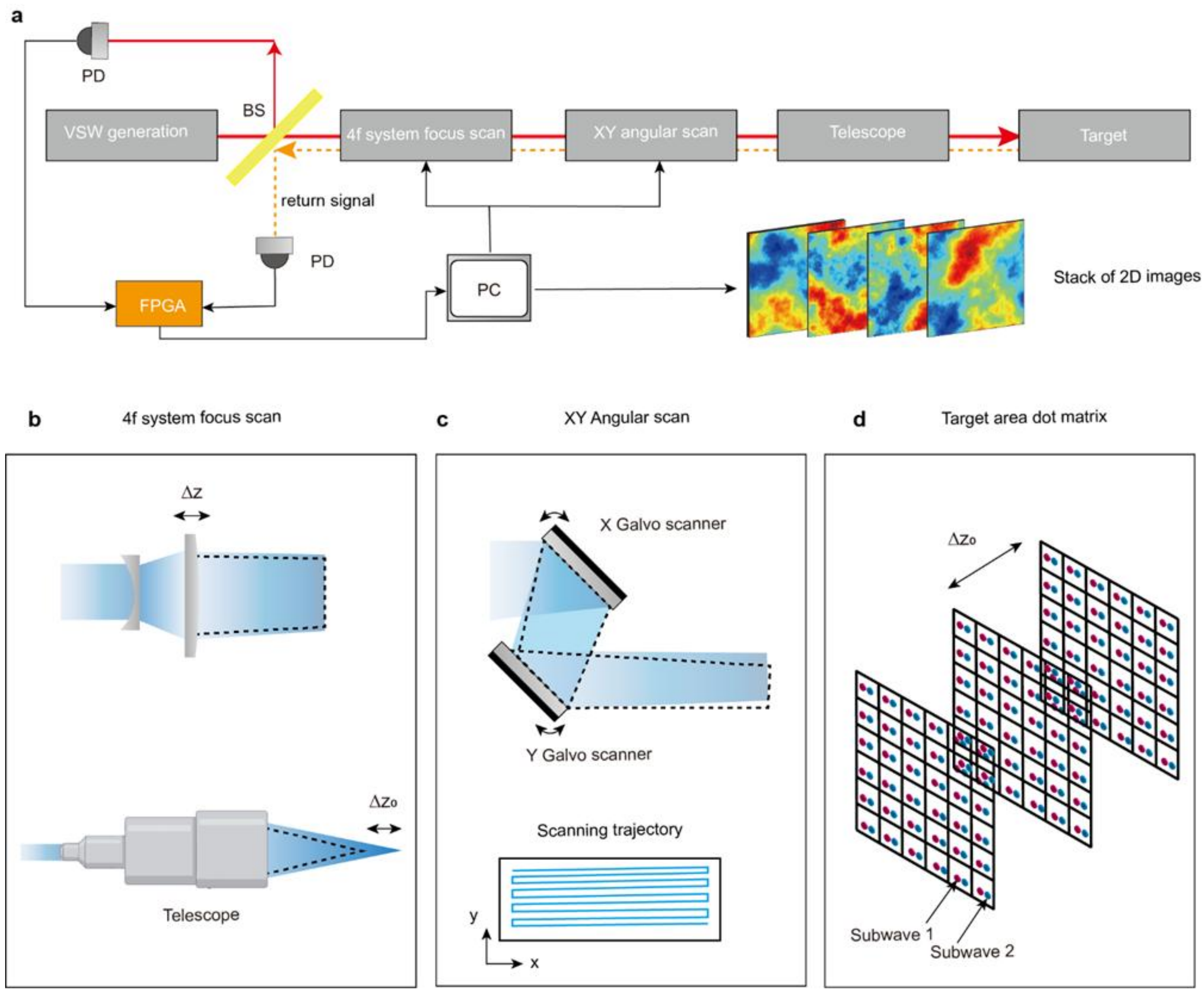

Fig. S1 | The architecture of real-time 3D measurement. a, Schematic of the experimental setup. A VSW generation module directs light to a beam splitter (BS), which divides it into two paths serving as the "local reference arm" and the "measurement arm". The signal beam propagates through a 4f-system focus-scan module and an XY angular-scan module, passes through a telescope, and reaches the target. The backscattered return signal (yellow dashed line) is collected by a photodetector (PD). Electrical signals are digitized using an integrated instrumentation platform. A computer is used to coordinate hardware commands and execute real-time data processing. **b,** Detail of the 4f-system focus-scan module. Top: The lens arrangement features an internal displacement, Δz. Bottom: The telescope output shows the resulting axial focal shift, Δz_o. **c,** Detail of the XY angular-scan module. Top: Orthogonal X- and Y- axis galvanometer scanners steer the beam. Bottom: The inset displays the user-defined scanning trajectory. **d,** Dot matrix of the target area. The volumetric sampling grid spans the axial range Δz_o, illustrating the spatial interleaving of measurement points labelled subwave 1 and subwave 2.

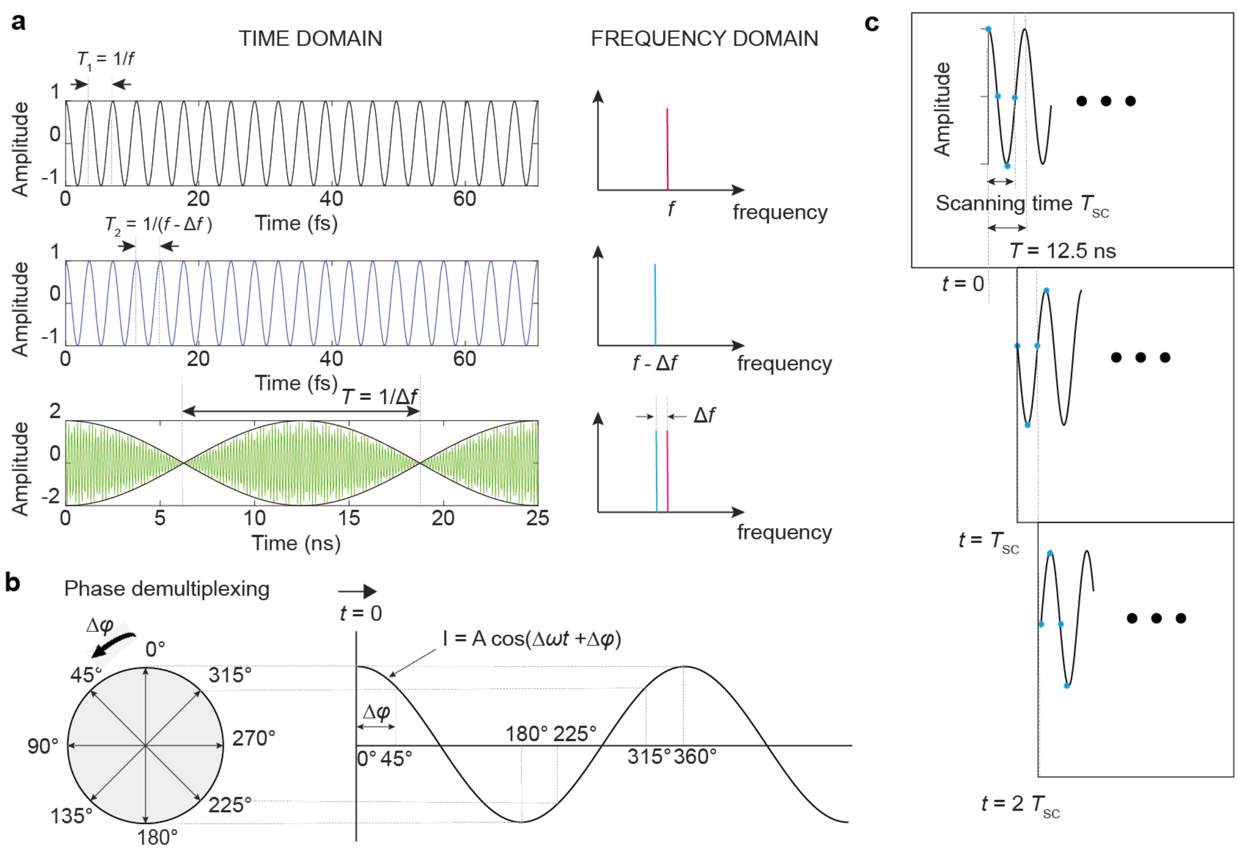

Fig. S2 | The temporal resolution analysis of VSDI. a, Time-domain waveforms (left) and corresponding spectra (right) of the vector synthetic wave (VSW) signal formed by two sub-waves with a frequency offset Δf, giving a beat period T. **b,** Schematic of phase demodulation, illustrating the relationship between the phase offset $\Delta\varphi$ and the corresponding intensity waveform. **c,** Timing diagram across three consecutive scanning cycles. T_{SC} defines the single-point acquisition window.

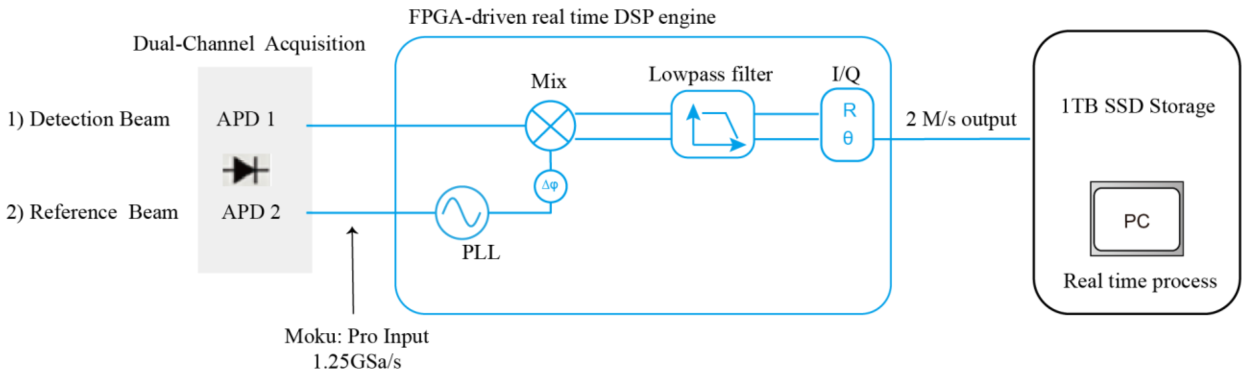

Fig. S3 | Schematic of the hardware-accelerated demodulation architecture.

Fig. S4 | Photograph of the integrated instrumentation platform.

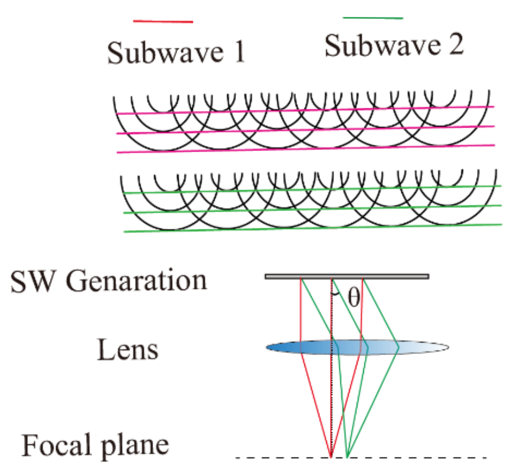

Fig. S5 | Illustration of the light path of VSDI.

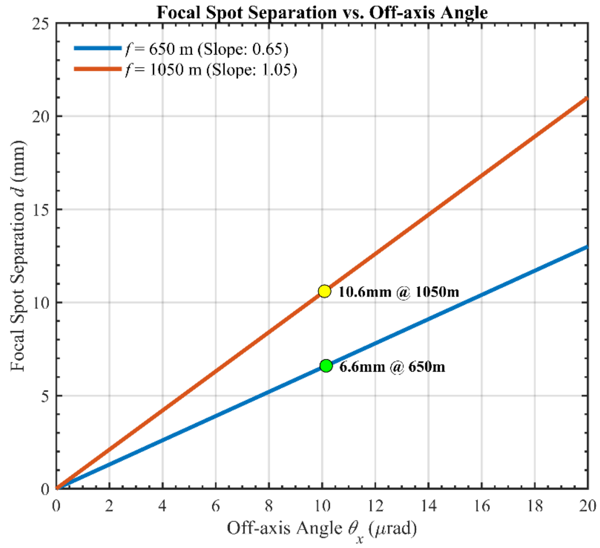

Fig. S6 | Simulation of the lateral spatial resolution. Simulated focal-spot separation d as a function of the off-axis tilt angle θ_x.

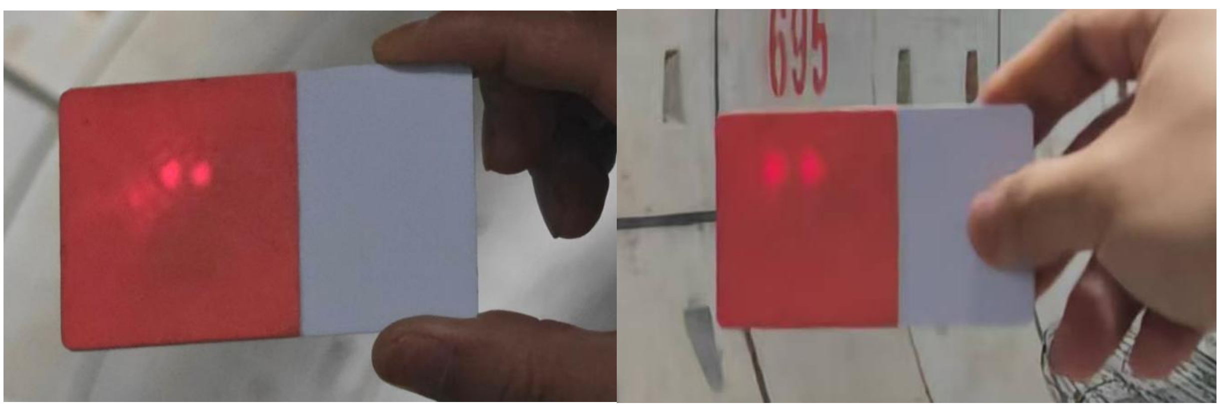

Fig. S7 | Measured focal spot morphology. (Left) Measured focal spot at 650 m. (Right) Measured focal spot at 1,050 m.

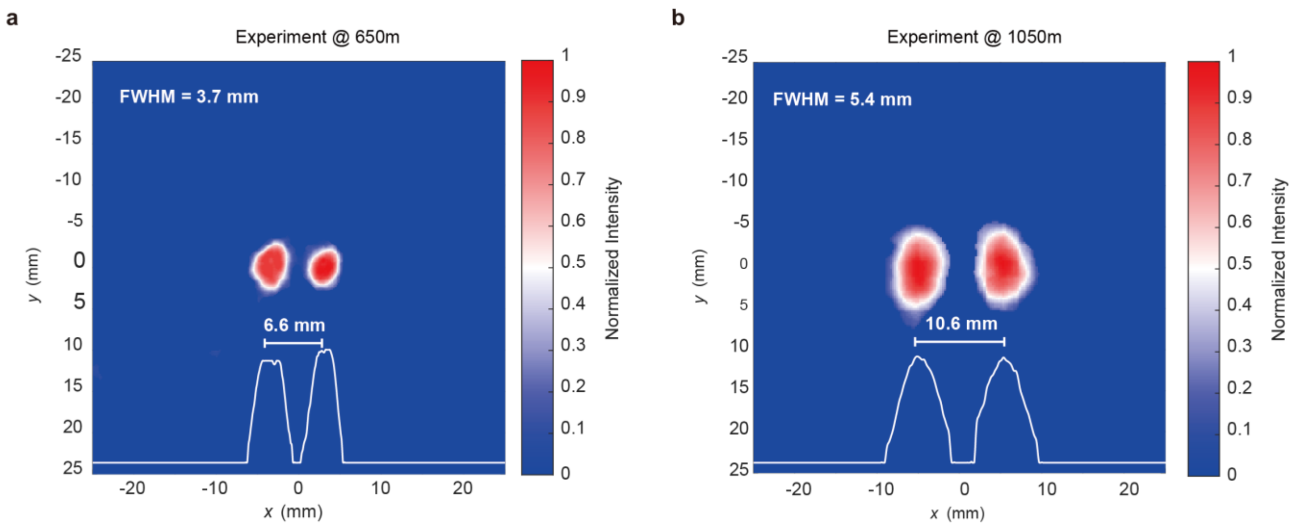

Fig. S8 | Experimental validation. a, Experimental transverse intensity profile measured at the focal plane (*z* = 650 m), resolving a spot separation of *d* = 6.6 mm. **b,** Experimental transverse intensity profile measured at the focal plane (*z* = 1,050 m), resolving a spot separation of *d* = 10.6 mm.

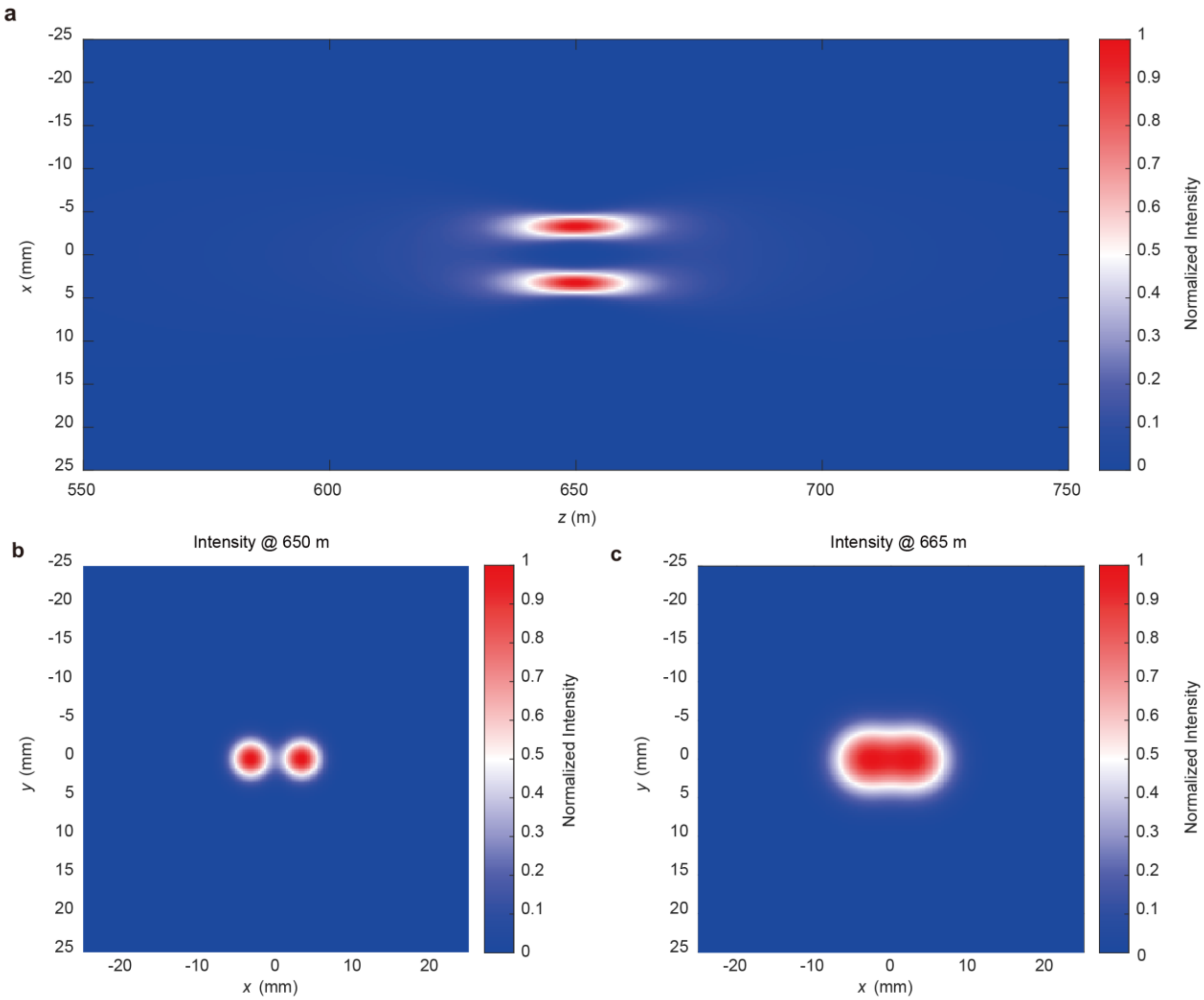

Fig. S9 | Numerical simulation of *f* = 650 m. a, Simulated *x*-*z* plane evolution of the dual-beam intensity distribution. **b,** Simulated transverse intensity profile at the focal plane. **c,** Transverse intensity profiles at the post-focal (z = 665 m) boundaries.

.

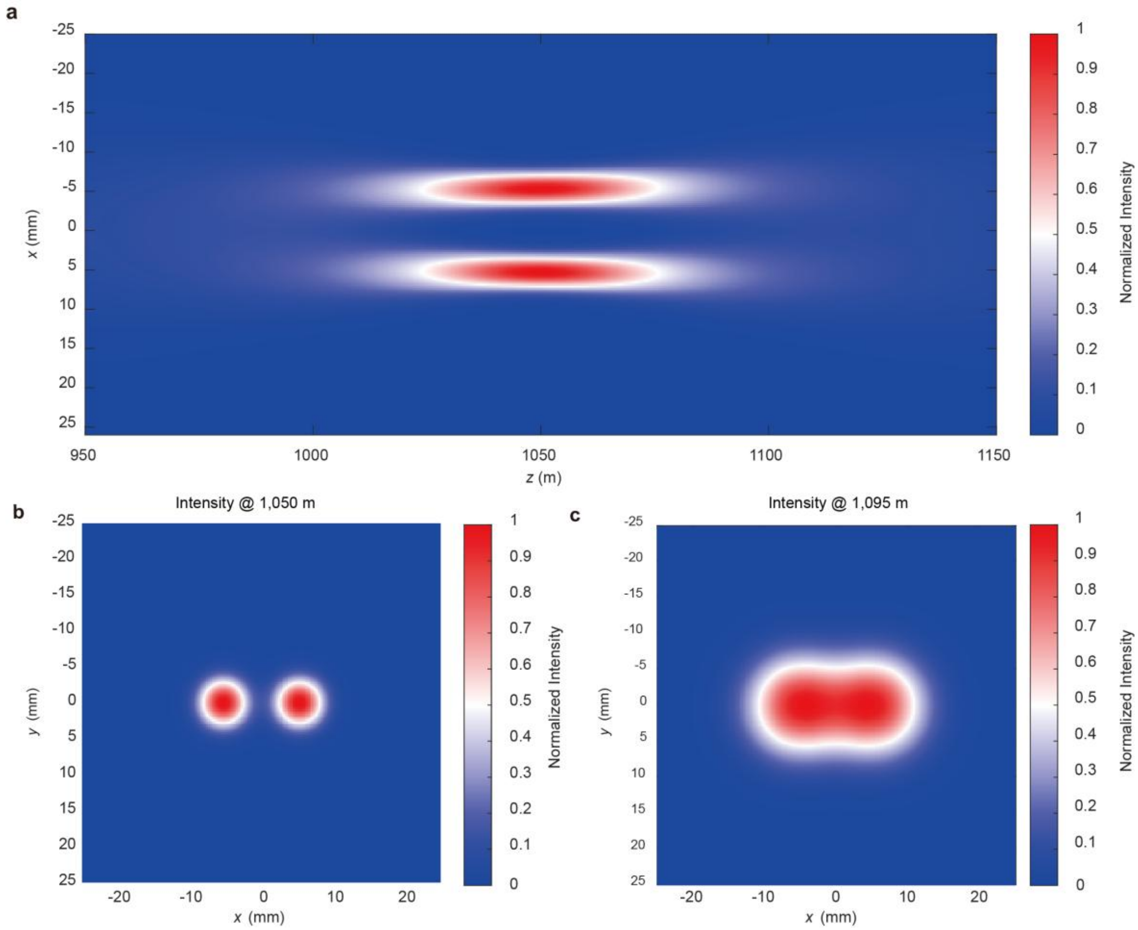

Fig. S10 | Numerical simulation of *f* = 1,050 m. a, Simulated *x*-*z* plane evolution of the dual-beam intensity distribution. **b,** Simulated transverse intensity profile at the focal plane. **c,** Transverse intensity profiles at the post-focal (z = 1,095 m) boundaries.

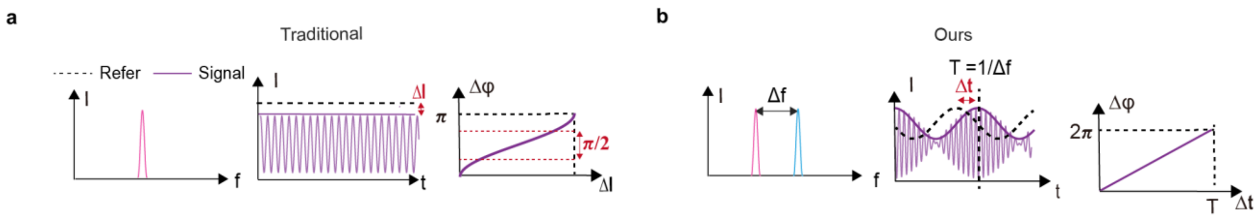

Fig. S11 | Theoretical concept of C-FLDI and VSDI. a, C-FLDI relies on intensity modulation ($I \propto \cos(\Delta\varphi)$), where the inherent cosine nonlinearity restricts the unambiguous measurement range to an interval of π/2. **b,** the probe signal in VSDI adopts a physically intuitive form, given by $I \propto \cos(\Delta\omega t+\Delta\varphi)$. This phase difference $\Delta\varphi$ spans the full 2π range and is reconstructed by continuously tracking the relative temporal shift Δt.

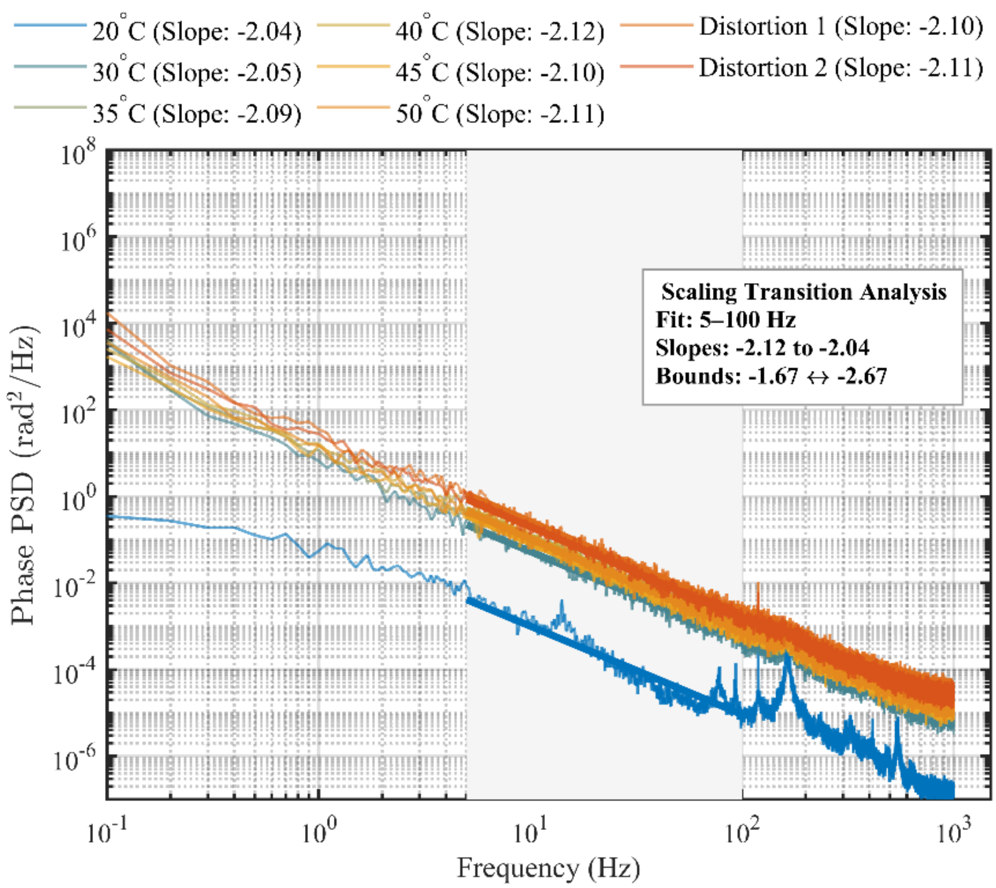

Fig. S12 | PSD analysis under varying convective regimes. The plot displays the Phase PSD as a function of frequency *f* under multiple thermal driving conditions and representative distortion scenarios. Experimental PSD curves are color-coded from cold (blue, 20°C) to hot (red, 50°C). Within the inertial subrange (shaded grey region), the measured slopes are shown in solid lines.

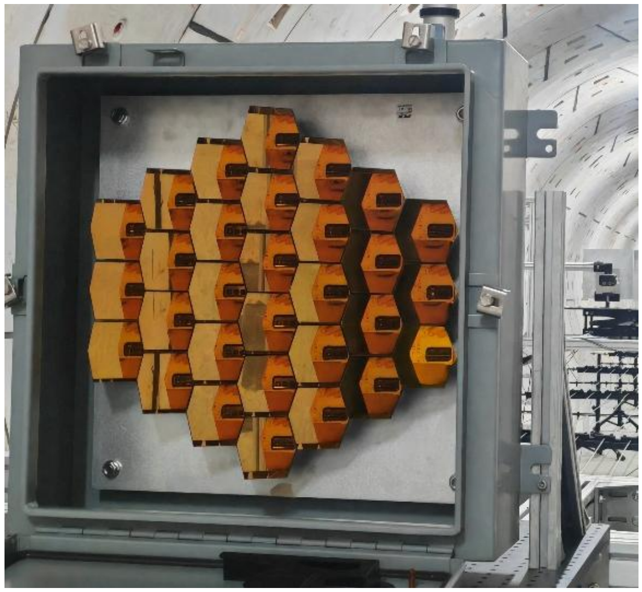

Fig. S13 | Photograph of corner cube retroreflector.

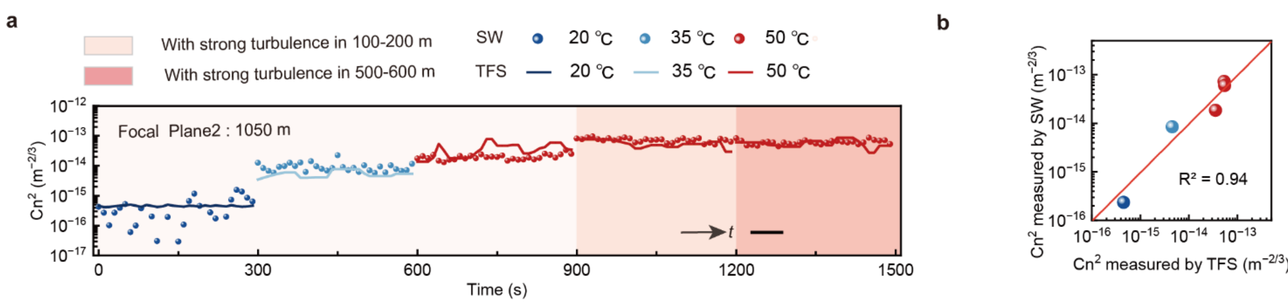

Fig. S14 | Long-term turbulence measurements. a, Turbulence measurements after mapping each temperature to its corresponding refractive-index structure constant. The solid circles denote SW measurements acquired at an update rate of 0.1 Hz. The solid lines denote the TFS measurements acquired at an update rate of 0.1 Hz. Shaded regions indicate the introduction of strong turbulence by heating off-focal segments along the propagation path to 50 °C. Scale bar, 1 min (horizontal). b, SW measurements after mapping each temperature to the corresponding median value. The red line represents the theoretical relationship between the SW and TFS measurements. R^2 denotes the coefficient of determination.

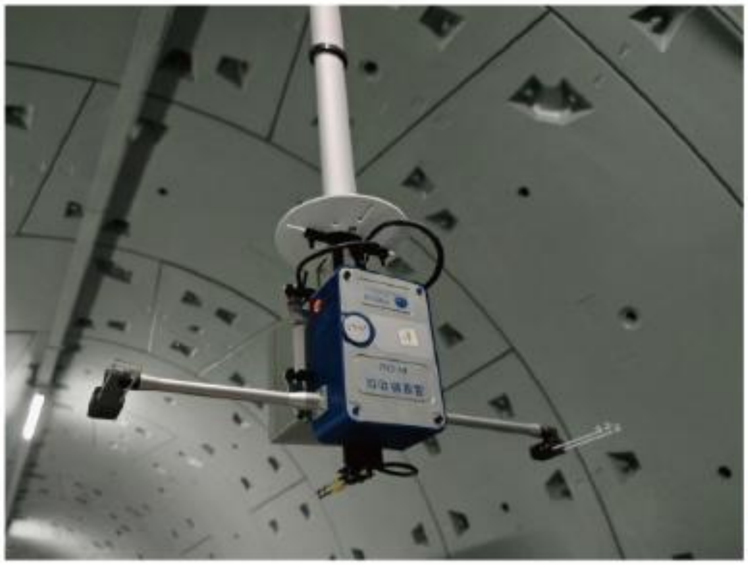

Fig. S15 | Photograph of temperature fluctuation sensor.

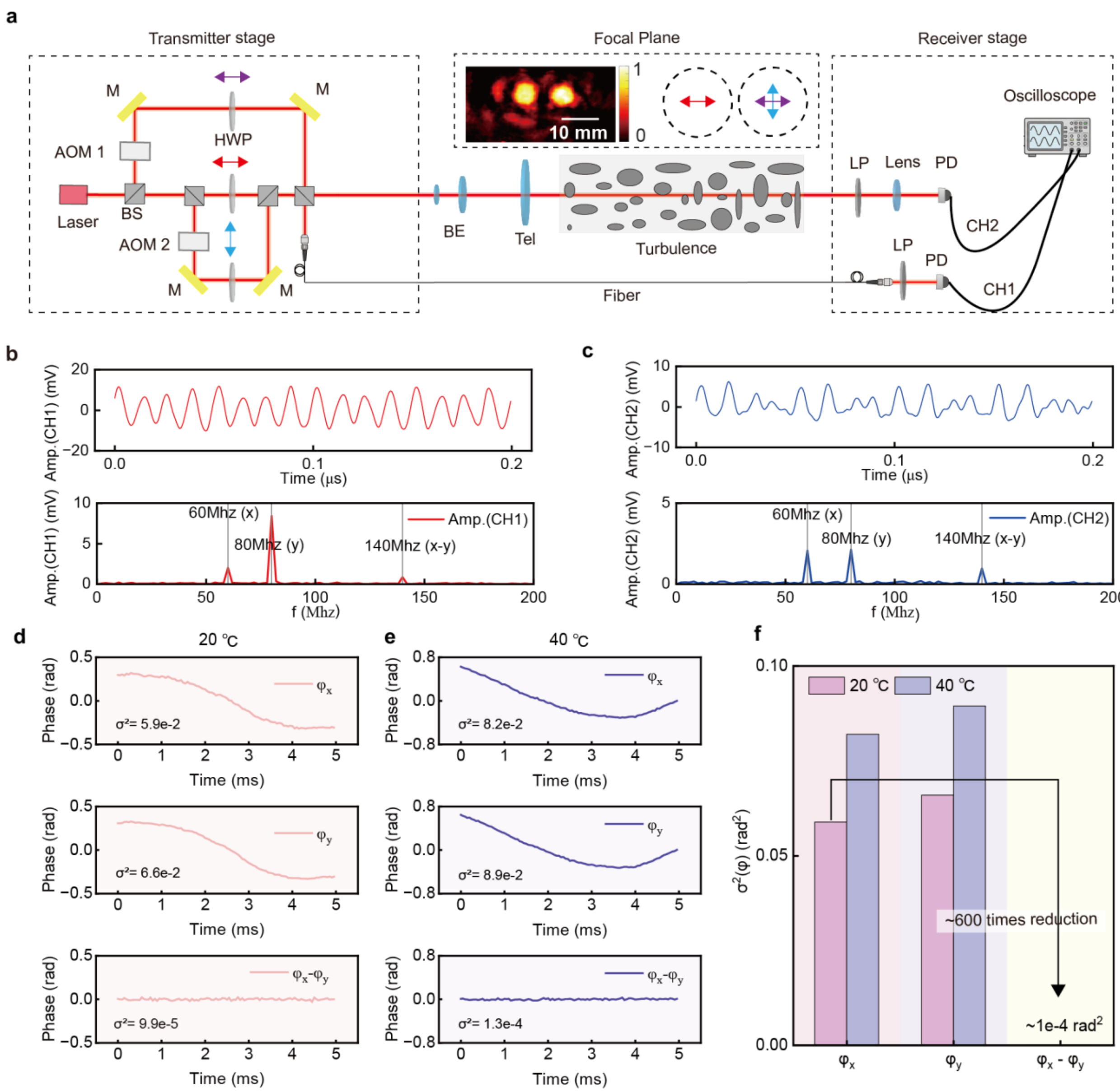

Fig. S16 | Polarization-resolved remote turbulence measurements enabled by frequency-domain demultiplexing. a, Experimental layout. The detection signal is recorded on CH2, while the fiber-end signal is simultaneously recorded on CH1 as a local reference. Two AOM-shifted probe components are transmitted through the turbulence path after beam expansion (BE) and telescope (Tel), and the two-channel waveforms are acquired by an oscilloscope. **b, c,** Representative time-domain traces (top) and Fourier spectra (bottom) of CH1 (b) and CH2 (c). Polarization channels are separated by isolating the corresponding heterodyne bands in the frequency domain from FFTs of the recorded waveforms, rather than by optical polarization splitting. **d, e,** Retrieved phase fluctuations for the x- and y-polarized channels (φ_x and φ_y) and their differential phase ($\varphi_x - \varphi_y$) at 20 °C (d) and 40 °C (e). **f,** Phase-variance comparison shows that the *x*- and *y*-polarized channels exhibit consistent trends, indicating an approximately polarization-isotropic turbulence response, whereas the differential channel directly measures the residual polarization dependence ($\varphi_x - \varphi_y$).